Weierstraß-Institut
für Angewandte Analysis und Stochastik
Leibniz-Institut im Forschungsverbund Berlin e. V.

Preprint ISSN 2198-5855

Challenges for drift-diffusion simulations of semiconductors: A comparative study of different discretization philosophies

Patricio Farrell[1], Dirk Peschka[2]

submitted: March 7, 2018

[1] TU Hamburg-Harburg
Institut für Mathematik
Am Schwarzenberg-Campus 3
21073 Hamburg, Germany
E-Mail: patricio.farrell@wias-berlin.de

[2] Weierstrass Institute
Mohrenstr. 39
10117 Berlin, Germany
E-Mail: dirk.peschka@wias-berlin.de

No. 2486
Berlin 2018

2010 *Mathematics Subject Classification.* 35Q99, 82D37, 65M08, 65M06, 65M60.

Key words and phrases. Finite volume method, finite element method, finite difference method, comparison, benchmark, flux discretization, Scharfetter-Gummel scheme, semiconductors, van Roosbroeck system, device simulation, nonlinear diffusion, diffusion enhancement.

This research is carried out in the framework of MATHEON supported by the Einstein Foundation Berlin.

Edited by
Weierstraß-Institut für Angewandte Analysis und Stochastik (WIAS)
Leibniz-Institut im Forschungsverbund Berlin e. V.
Mohrenstraße 39
10117 Berlin
Germany

Fax: +49 30 20372-303
E-Mail: preprint@wias-berlin.de
World Wide Web: http://www.wias-berlin.de/

Challenges for drift-diffusion simulations of semiconductors: A comparative study of different discretization philosophies

Patricio Farrell, Dirk Peschka

Abstract

We analyze and benchmark the error and the convergence order of finite difference, finite-element as well as Voronoï finite-volume discretization schemes for the drift-diffusion equations describing charge transport in bulk semiconductor devices. Three common challenges, that can corrupt the precision of numerical solutions, will be discussed: boundary layers at Ohmic contacts, discontinuties in the doping profile, and corner singularities in L-shaped domains. The influence on the order of convergence is assessed for each computational challenge and the different discretization schemes. Additionally, we provide an analysis of the inner boundary layer asymptotics near Ohmic contacts to support our observations.

1 Introduction

Over the past decades many different methods have been proposed to solve the semiconductor device equations numerically. Today, most commonly variants of the finite volume method (FV) are used. However, also discretization schemes based on finite element methods or finite difference methods (FD) have been developed in the past or are presently used. The finite volume method became very popular after Scharfetter and Gummel published their seminal paper [26] in 1969. For Boltzmann statistics, their scheme can easily deal with the convection-dominated nature of these equations. Even though Scharfetter and Gummel solved the van Roosbroeck system only in one spatial dimension and interpreted their method as a finite difference scheme, others quickly realized that in several space dimensions it is beneficial to translate their scheme into a finite volume setting [4, 3, 27].

Only recently thermodynamically consistent schemes have been proposed to handle non-Boltzmann statistics as well [7, 21, 14, 15, 23]. A key indicator to measure how well the semiconductor can be described by Boltzmann statistics is the diffusion enhancement [22, 24]. The more the diffusion enhancement differs from unity, the less accurate it is to assume Boltzmann statistics. For crystalline semiconductors assuming Boltzmann statistics becomes inaccurate for large densities, *e.g.*, due to high doping or low temperatures [17]. For organic semiconductors this effect becomes already dominant for low or moderate densities [22]. For this reason we limit ourselves in the present work to a diffusion-enhanced flux discretization scheme [7, 21].

The finite element method is probably the most prominent approach to compute solutions of partial differential equations that arise in the natural sciences [10, 12, 8, 28]. It works on general meshes, allows for a systematic error analysis and a systematic control over the approximation degree, by choosing the polynomial degree of elements when the regularity of the solution admits. It is also popular for convection-dominated problems [20]. For this reason variants of the finite element method have been applied to the van Roosbroeck system as well [2, 4, 6, 9, 31]. Most of the authors use the electron and hole densities in the weak formulation. Auf der Maur proposed to use the quasi-Fermi potentials as primary variables instead [1].

DOI 10.20347/WIAS.PREPRINT.2486 Berlin 2018

Despite their popularity, to the best of our knowledge neither for finite volume nor for finite element discretizations of the basic semiconductor device equations comparative convergence studies have been undertaken, which would be particularly important in situations with nontrivial distribution functions. The present paper aims at bridging this gap and provides a study of different discretization philosophies and also allows to compare how these approaches cope with different challenges. We focus on the more difficult case of non-Boltzmann statistics and use quasi-Fermi potentials as independent variables. Ohmic contacts will be treated by assuming pointwise electroneutrality and equality of the quasi-Fermi potentials at the contact, *i.e.*, Dirichlet conditions. This approach is very common in the literature, *e.g.*, [27, 17], even though it introduces logarithmic boundary layers at these contacts which we will derive.

We study three major challenges for any discretization scheme, that influence the error and convergence rate of the numerical solutions: i) boundary layers, ii) discontinuous doping and iii) corner singularities. For any generic numerical method steep boundary layers usually introduce numerical problems leading to poor or even missing convergence. Often, this issue is addressed by resolving the length scale of the boundary layer in the mesh using boundary adapted meshes [25, 29]. To understand the feasibility of resolving the length scale, we analyze the boundary layer near the Ohmic contacts using an inner leading-order expansion of a matched asymptotic expansion for the quasi-Fermi potentials. Realistic semiconductor devices are heterostructures, where the doping is usually modeled as a piecewise constant function. This discontinuity in the data, however, can lead to slower convergence which we examine as well. Finally, we study how an L-shaped domain impacts the convergence order of the solutions due to the occurrence of corner singularities.

In the following section, we introduce the basic semiconductor device equations, the van Roosbroeck system, nondimensionalize it as well as state and solve the leading order inner problem for boundary layers in the quasi-Fermi potentials near Ohmic contacts. In Section 3 we provide specific details for the spatial discretization of the van Roosbroeck system, *i.e.*, using finite differences, finite elements, and Scharfetter-Gummel type finite volume methods. The influence of the boundary layers at Ohmic contacts as well as the impact of the smoothness of the doping is examined with the help of a 1D problem in Section 4. In Section 5 we then compare how the different discretization schemes handle a 2D L-shaped domain and study the influence of boundary layers and corner singularities on the convergence order in more detail. The simulation data presented in this work is also published [16] and can be used for comparative benchmark studies.

2 The van Roosbroeck system

2.1 The model

The van Roosbroeck system is a drift-diffusion model, which describes the recombination and transport of charge carriers driven by diffusion and by electric fields within a semiconductor device. It consists of three nonlinear, coupled partial differential equations for the electrostatic potential $\psi : \Omega \to \mathbb{R}$ as well as the non-negative electron and hole densities $n : \Omega \to \mathbb{R}^+$ and $p : \Omega \to \mathbb{R}^+$, namely a Poisson equation and two continuity equations. We consider a homogeneous material and some domain $\Omega \subseteq \mathbb{R}^d$ for $d \in \{1, 2, 3\}$ in an isothermal setting. Then the stationary van Roosbroeck system

is given by the system of elliptic partial differential equations

$$-\nabla \cdot (\varepsilon_0 \varepsilon_r \nabla \psi) = q\,(C + p - n)\,, \tag{1a}$$

$$\nabla \cdot \mathbf{j}_n = +qR, \tag{1b}$$

$$\nabla \cdot \mathbf{j}_p = -qR, \tag{1c}$$

where q denotes the elementary charge, ε_0 is the vacuum permittivity and ε_r is the relative permittivity of the material, see Tab. 6. The recombination rate R and the charge-carrier currents $\mathbf{j}_n, \mathbf{j}_p$ depend on the solution n, p, ψ and vanish in thermal equilibrium. The doping concentration $C\colon \Omega \to \mathbb{R}$ varies spatially and can have discontinuities. The equations of state are given by

$$n(\eta_n) = N_c \mathcal{F}\big(\eta_n\big), \qquad \eta_n(\psi, \varphi_n) = \frac{q(\psi - \varphi_n) - E_c}{k_B T}, \tag{2a}$$

$$p(\eta_p) = N_v \mathcal{F}\big(\eta_p\big), \qquad \eta_p(\psi, \varphi_p) = \frac{q(\varphi_p - \psi) + E_v}{k_B T}, \tag{2b}$$

where the statistical distribution function $\mathcal{F}$ relates the electron and hole densities n, p to the corresponding electrochemical potentials φ_n, φ_p, which are also known as quasi-Fermi potentials.

There are computational and modeling advantages to using the quasi-Fermi potentials. For instance, their variation in magnitude is considerably smaller than that of the corresponding densities and the equation of state automatically implies non-negativity of the density. At least across certain heterojunctions the quasi-Fermi potentials are continuous, whereas the densities will usually be discontinuous. Furthermore, since the quasi-Fermi potentials are the thermodynamic quantities, whose gradients and differences are driving the charge transport and recombination rates, a formulation based on these is easier to model from a thermodynamic point-of-view. This is why we focus on quasi-Fermi potentials and electrostatic potential as the set of unknowns in this paper. Furthermore, we set the recombination rate to zero as it plays a minor role for most of our considerations.

The effective density of states for electrons in the conduction band N_c and holes in the valence band N_v as well as the corresponding band-edge energies E_c, E_v and the band gap $E_g = E_c - E_v$ are material parameters and assumed to be spatially constant in this paper. Temperature and the Boltzmann constant are denoted with T and k_B. The three most important reference cases for the statistical distribution functions are the Boltzmann, Blakemore and Fermi-Dirac function, denoted by

$$\mathcal{F}(\eta) = \exp(\eta), \tag{3a}$$

$$\mathcal{F}(\eta) = (\exp(-\eta) + \gamma)^{-1}, \tag{3b}$$

$$\mathcal{F}(\eta) = F_\alpha(\eta). \tag{3c}$$

For example, the behavior of three-dimensional bulk semiconductors is described most accurately using the Fermi-Dirac-Integral F_α with index $\alpha = 1/2$. For large negative arguments the $F_{1/2}$ can be approximated by either of the other two functions since they all share an exponential Boltzmann tail. By choosing the parameter $\gamma = 0.27$, the Blakemore function (3b) approximates $F_{1/2}$ fairly accurately up to $\eta \leq 1.5$. For each distribution function, the corresponding current densities in (1b) and (1c) are defined by

$$\mathbf{j}_n = -q\mu_n n \nabla \varphi_n = -q\mu_n n \nabla \psi + qD_n \nabla n, \tag{4a}$$

$$\mathbf{j}_p = -q\mu_p p \nabla \varphi_p = -q\mu_p p \nabla \psi - qD_p \nabla p. \tag{4b}$$

Using the thermal voltage $U_T = \frac{k_B T}{q}$, the diffusion coefficients D_n, D_p are linked to the carrier mobilities μ_n, μ_p via a generalized Einstein relation

$$\frac{D_n}{\mu_n} = U_T\, g\big(\eta_n\big), \qquad \frac{D_p}{\mu_p} = U_T\, g\big(\eta_p\big), \tag{5a}$$

the diffusion enhancement g is defined by

$$g(\eta) = \frac{\mathcal{F}(\eta)}{\mathcal{F}'(\eta)} \tag{5b}$$

as motivated in [30]. For the Boltzmann function (3a), we immediately see that $g \equiv 1$, which gives the classical Einstein relation $D_n = \mu_n U_T$. For the Blakemore function (3b), we have $g(\eta) = 1+\gamma\exp(\eta)$.

The system (1) is supplied with mixed Dirichlet-Neumann boundary conditions. We will briefly discuss the case where the boundary of the domain Ω can be decomposed into Ohmic contacts (Γ_α) and an insulating interface (Γ), *i.e.*,

$$\partial\Omega = \Gamma \cup \bigcup_{\alpha=1}^{N_\mathsf{o}} \Gamma_\alpha.$$

Ideal semiconductor-metal interfaces, such as Ohmic contacts, are modeled by Dirichlet boundary conditions, where we require a local charge neutrality $C + p - n = 0$ and a local equilibrium $\varphi_n = \varphi_p$, where outside thermodynamic equilibrium the value of the quasi-Fermi potential might be different on each Γ_α. For any Ohmic contact Γ_α with $\alpha = 1, \dots, N_\mathsf{o}$, we set

$$\psi(\mathbf{x}) = \psi_\mathsf{bi}(\mathbf{x}) + U_\alpha, \tag{6a}$$
$$\varphi_n(\mathbf{x}) = U_\alpha, \qquad \text{for all } \mathbf{x} \in \Gamma_\alpha \tag{6b}$$
$$\varphi_p(\mathbf{x}) = U_\alpha, \tag{6c}$$

where U_α denotes the corresponding externally applied contact voltage and $U_\alpha \equiv 0$ in equilibrium. These Dirichlet conditions for the potentials correspond to Dirichlet conditions for the densities, which we denote by $n(\mathbf{x}) = n_\alpha$ and $p(\mathbf{x}) = p_\alpha$ for all $\mathbf{x} \in \Gamma_\alpha$. The built-in potential ψ_bi at the boundary is defined by the pointwise charge neutrality

$$0 = N_v \mathcal{F}\Big(\frac{E_v - q\psi_\mathsf{bi}(\mathbf{x})}{k_B T}\Big) - N_c \mathcal{F}\Big(\frac{q\psi_\mathsf{bi}(\mathbf{x}) - E_c}{k_B T}\Big) + C(\mathbf{x}).$$

While for the Boltzmann function monotonicity ensures that such a ψ_bi always exists, for the Blakemore function charge neutrality can only be attained at points $\mathbf{x} \in \Omega$ where the doping satisfies $-N_v < \gamma C(\mathbf{x}) < N_c$. We just remark, that in general, this equation yields no closed-form solution, and therefore needs to be computed numerically. The boundary conditions for the more advanced nonlinear semiconductor-metal interfaces such as Schottky contacts or gate contacts can be found in [27, 17]. On the remaining non-charged, insulating interfaces we impose (natural) homogeneous Neumann boundary conditions

$$\nabla\psi(\mathbf{x}) \cdot \boldsymbol{\nu} = \mathbf{j}_n(\mathbf{x}) \cdot \boldsymbol{\nu} = \mathbf{j}_p(\mathbf{x}) \cdot \boldsymbol{\nu} = 0 \qquad \text{for all } \mathbf{x} \in \Gamma, \tag{6d}$$

where $\boldsymbol{\nu}$ denotes the outward-pointing normal vector to the interface. Finally, we present an argument why the Boltzmann distribution function for the minority charge carriers is accurate near Ohmic contacts even if in the interior a non-Boltzmann distribution function is used. First note that most distribution functions, and in particular those in (3), satisfy $\mathcal{F}(\eta) \leq \exp(\eta)$. Then, for a doping concentration $C < 0$, we use charge neutrality and the shift $\psi_\mathsf{bi} = q^{-1}E_c - U_T w$ to estimate

$$0 = N_v \mathcal{F}(-\tfrac{E_g}{k_B T} + w) - N_c \mathcal{F}(-w) + C \leq N_v \exp(-\tfrac{E_g}{k_B T} + w) + C, \tag{7}$$

which implies $w \geq \log(-C/N_v) + E_g/(k_B T)$. Assuming $E_g \gg k_B T$ and $|C| \sim N_v$ we finally get $w \gg 1$. A similar argument for $C > 0$ shows that the Boltzmann distribution is a good approximation $\mathcal{F}(w) \sim \exp(w)$ for the equation of state of the minority charge density near Ohmic contacts when $|C| \sim N_c$ and $E_g \gg k_B T$.

2.2 Non-dimensionalization

Now we present the non-dimensionalization of the van Roosbroeck system (1), which will also motivate the following boundary layer analysis. First we introduce the scalings,

$$\mathbf{x} \to \ell\,\widetilde{\mathbf{x}}, \quad \psi \to U_T\widetilde{\psi}, \quad \varphi_{n,p} \to U_T\widetilde{\varphi}_{n,p}, \quad (n,p,C) \to (\rho\,\widetilde{n}, \rho\,\widetilde{p}, \rho\,\widetilde{C}),$$

so that we obtain the scaled van Roosbroeck system

$$-\tilde{\nabla}^2\widetilde{\psi} = \frac{\ell^2}{\lambda^2}(\widetilde{C} + \widetilde{p} - \widetilde{n}), \qquad \tilde{\nabla}\cdot\widetilde{\mathbf{j}}_n = +\frac{q\ell}{J}R, \qquad \tilde{\nabla}\cdot\widetilde{\mathbf{j}}_p = -\frac{q\ell}{J}R, \tag{8}$$

with the non-dimensional currents $\tilde{\mathbf{j}}_n = -\bar{\mu}_n\tilde{n}\tilde{\nabla}\tilde{\varphi}_n$ and $\tilde{\mathbf{j}}_p = -\bar{\mu}_p\tilde{p}\tilde{\nabla}\tilde{\varphi}_p$, where we introduced the reduced mobilities $\bar{\mu}_n = \mu_n/\mu$ and $\bar{\mu}_p = \mu_p/\mu$. Additionally, we also introduce the length scale λ and the current density J

$$\lambda^2 = \frac{\varepsilon_0\varepsilon_r U_T}{q\rho}, \qquad J = \frac{q\mu\rho U_T}{\ell}. \tag{9}$$

We will make specific choices for the characteristic density ρ in the next section. Note that, λ is interpreted as a screening length, whereas in the context of electrolytes J is related to the classical diffusion-limited current density of Nernst, *e.g.*, [5].

When J is set to a typical current value for a given bias V_{ext}, then (9) defines two length scales λ and ℓ, which compete with the *device length scale* in the van Roosbroeck system (8). We denote the device length scale with L. We have $0 < \lambda \ll L$ for large densities ρ, whereas $0 < \ell \ll L$ holds for small densities ρ or for large currents J.

Before we can bring forward an argument about the ordering of the length scales, we need to determine the characteristic density scale ρ. First, the Debye length λ_D is the characteristic length scale, on which deviations from electroneutrality are observed, and typical values for λ_D are in the range of $1\,\mathrm{nm}$ to $100\,\mathrm{nm}$. As the screening of charges is dictated by the doping, it makes sense to define

$$C_{\mathsf{m}} = \max_{\mathbf{x}\in\Omega} |C(\mathbf{x})|, \tag{10}$$

and then to specify $\rho = C_{\mathsf{m}}$ for λ in (9), so that the Debye screening length is

$$\lambda_D^2 = \frac{\varepsilon_0\varepsilon_r U_T}{qC_{\mathsf{m}}}. \tag{11}$$

Second, at Ohmic contacts Γ_α where (7) holds for the minority charge density, the corresponding boundary condition is determined from the Ohmic contacts for Boltzmann statistics, which are

$$n_\alpha = \frac{1}{2}\Big(+C + \big(C^2 + 4N_i^2\big)^{\frac{1}{2}}\Big) \quad \text{or} \quad p_\alpha = \frac{1}{2}\Big(-C + \big(C^2 + 4N_i^2\big)^{\frac{1}{2}}\Big), \tag{12}$$

where $N_i^2 = N_c N_v \exp(-E_g/(k_B T))$. For simplicity we will assume $C = \pm C_{\mathsf{m}}$ at the boundary. The previous assumptions leading to (7) also imply $N_i \ll C_{\mathsf{m}}$, so that to leading order we can expand

$$n_\alpha = \begin{cases} N_i^2/C_{\mathsf{m}} & C < 0 \\ C_{\mathsf{m}} & C > 0 \end{cases}, \qquad p_\alpha = \begin{cases} C_{\mathsf{m}} & C < 0 \\ N_i^2/C_{\mathsf{m}} & C > 0 \end{cases}. \tag{13}$$

We are going to discuss the case $C < 0$, where $\delta = N_i/C_\mathsf{m} \ll 1$ and $n_\alpha = N_i^2/C_\mathsf{m} = C_\mathsf{m}\delta^2$, *i.e.*, electrons are the minority carriers. If we use $\rho = n_\alpha$ in the scaling for J in (9) then we can define the boundary layer thickness ℓ_J via

$$\ell_J = \frac{q\mu n_\alpha U_T}{J} = \frac{q\mu C_\mathsf{m} U_T}{J}\delta^2. \tag{14}$$

If we are interested in situations with $\ell_J \ll \lambda_D$, this requires $J \gg J_\mathsf{lim}$, with the intrinsic limiting current J_lim defined as

$$J_\mathsf{lim} = \frac{q\mu n_\alpha U_T}{\lambda_D} = \frac{q^2\mu N_i^2}{\varepsilon_0\varepsilon_r}\lambda_D. \tag{15}$$

We get surprisingly low intrinsic limiting currents for typical semiconductors and typical Debye lengths, see Table 1.

material	N_i	μ_n	ε_r	limiting current density J_lim
Si	$10^{10}\mathrm{cm}^{-3}$	$1400\,\mathrm{cm}^2/\mathrm{Vs}$	11.7	$3.5 \cdot 10^{-13}\,\mathrm{kA/cm}^2 \cdot \lambda_D[\mathrm{nm}]$
Ge	$10^{13}\mathrm{cm}^{-3}$	$3900\,\mathrm{cm}^2/\mathrm{Vs}$	16.2	$7.0 \cdot 10^{-7}\,\mathrm{kA/cm}^2 \cdot \lambda_D[\mathrm{nm}]$
GaAs	$10^{6}\mathrm{cm}^{-3}$	$8500\,\mathrm{cm}^2/\mathrm{Vs}$	12.9	$1.9 \cdot 10^{-20}\,\mathrm{kA/cm}^2 \cdot \lambda_D[\mathrm{nm}]$

Table 1: Typical values of J_lim for semiconductors at $T = 300\mathrm{K}$.

2.3 Boundary layer expansion

We are going to present a concise argument for the existence of boundary layers for the quasi-Fermi potential corresponding to the minority carrier density at Ohmic contacts Γ_α. We have already discussed that near Ohmic contacts the Boltzmann approximation is valid for the minority charge carriers. In order to show and solve the leading order inner expansion for the matched asymptotic expansion of the van Roosbroeck system, assume that the length scales are ordered as follows

$$0 < \ell_J \ll \lambda_D \ll L, \tag{16}$$

showing that an asymptotic expansion would require multiple layers to succeed. We will show that once the current density at an Ohmic contact becomes larger than the intrinsic limiting current, logarithmic boundary layers will appear in the quasi-Fermi potential of the corresponding minority carriers. To show this, we examine the leading order asymptotic problem as $\delta = N_i/C_m \to 0$, when the scales for the doping C_m, current J, and Debye length λ_D are fixed. After dropping the tilde symbols in the rescaled van Roosbroeck equations (8) and using (14), the problem reads

$$-\nabla^2\psi = \delta^4 \left(\frac{q\mu C_\mathsf{m} U_T}{J\lambda_D}\right)^2 (C + p - n), \tag{17a}$$

$$-\nabla \cdot \bar{\mu}_n n \nabla\varphi_n = \delta^2 \left(\frac{q^2\mu C_\mathsf{m} U_T}{J^2}\right) R, \tag{17b}$$

with the rescaled Ohmic contact $n = n_\alpha = 1$. We expand the solutions using

$$\psi = \psi^0 + \delta\psi^1 + \ldots, \qquad \varphi_n = \varphi_n^0 + \delta\varphi_n^1 + \ldots,$$

and obtain the leading order problem

$$-\nabla^2\psi^0 = 0, \tag{18a}$$
$$-\nabla\cdot\bar{\mu}_n n^0\nabla\varphi_n^0 = 0, \tag{18b}$$

where $n^0 = \bar{N}_c\exp(\eta_n^0)$, $\eta_n^0 = \psi^0 - \varphi_n^0 - E_c/(k_BT)$, and $\bar{N}_c = N_c/\rho$. Assuming the Ohmic contact Γ_α is located at $x = 0$, the explicit solution is given by

$$\psi^0(x) = \psi_\alpha + \xi x. \tag{19}$$

where the constant $\xi \ll 1$ remains to be determined by matching to an outer solution at the length scale λ_D. For the quasi-Fermi potential we solve an equivalent problem in densities, which can be reduced to the 1D problem

$$\partial_x j_n = \bar{\mu}_n\partial_x\big(\partial_x n^0 - n^0\partial_x\psi^0\big) = 0, \tag{20}$$

and has the exact solution

$$n^0(x) = n_\alpha\exp(\xi x) + \frac{j_n}{\xi\bar{\mu}_n}\left(\exp(\xi x) - 1\right) \tag{21}$$

with rescaled $n^0(0) = n_\alpha = 1$ and integration constant j_n. Using the equation of state $n^0 = \bar{N}_c\exp(\psi^0 - \varphi_n^0 - \frac{E_c}{k_BT})$, the electron quasi-Fermi potential is

$$\begin{aligned}\varphi_n^0(x) &= \psi^0(x) - \log\left(\frac{n^0(x)}{\bar{N}_c}\right) - \frac{E_c}{k_BT}\\ &\approx \psi^0(x) - \log\left(\frac{n_\alpha}{\bar{N}_c}(1+\xi x) + \frac{j_n x}{\bar{\mu}_n\bar{N}_c}\right) - \frac{E_c}{k_BT}\\ &\approx \psi^0(x) - \log\left(\frac{\varepsilon + x}{\varepsilon}\right) - \log\left(\frac{n_\alpha}{\bar{N}_c}\right) - \frac{E_c}{k_BT}\end{aligned}$$

where $\varepsilon = \bar{\mu}_n n_\alpha/j_n$ and we approximated using $\xi \ll 1$ several times. When we define the inner length scale ℓ_J via the dimensional electron current $J = j_n$, then we have $\varepsilon = 1$. In the original dimensional outer coordinates, when all quantities are represented in their original scales, we obtain the following leading order the expansion

$$\begin{aligned}\varphi_n^0(x) &= U_T\widetilde{\varphi}_n^0(\ell_J^{-1}x)\\ &= \psi^0(x) - U_T\log\left(\frac{\ell_J + x}{\ell_J}\right) + U_T\log\left(\frac{n_\alpha}{N_c}\right) - \frac{E_c}{q}.\end{aligned} \tag{22}$$

This shows that once the current density at an Ohmic contact J exceeds the intrinsic limiting current J_{lim}, then the quasi-Fermi potential of the minority carriers develops a logarithmic boundary layer of size ℓ_J, where

$$0 < \ell_J = \frac{J_{\text{lim}}}{J}\lambda_D \ll \lambda_D, \tag{23}$$

and the electrostatic potential ψ can be approximated by an affine function in this region. The boundary layer analysis of φ_p is entirely analogous.

3 Standard discretizations using potentials

In the following we are going to explain standard discretization methods to solve the van Roosbroeck system. In one spatial dimension we use a second-order finite difference (FD) method, whereas in two spatial dimensions we use a P_1 finite element (FE) method. We will compare these discretizations with a Voronoï finite volume (FV) method. All three methods formulated in terms of the quasi-Fermi potentials as primary variables, which transforms the convection-dominated drift-diffusion problem into a nearly degenerate elliptic system. The advantage of this approach is that quasi-Fermi potentials, also known as electro-chemical potentials, are the natural variables from a thermodynamic point of view. Additionally, it is easier to control the behavior of solutions at heterointerfaces using these variables. For all the discretization schemes the final nonlinear system of equations is solved using Newton's method.

In the following we collect the three different components of the solution in the vector-valued function $\mathbf{u} = (\psi, \varphi_n, \varphi_p) \colon \Omega \to \mathbb{R}^3$. Evaluating this function at a specific point $\mathbf{x} \in \Omega$ gives the vector $\mathbf{u}(\mathbf{x}) = \big(\psi(\mathbf{x}), \varphi_n(\mathbf{x}), \varphi_p(\mathbf{x})\big) \in \mathbb{R}^3$. Analogously, we denote the discrete solution with $\mathbf{u}^h = (\psi^h, \varphi_n^h, \varphi_p^h) \in \mathbb{R}^{N\times 3}$, where N is the number of degrees of freedom for each component. The three columns of the matrix $\mathbf{u}^h$ correspond to the three components of the solution, while the kth row of $\mathbf{u}^h$ approximates the solution at a point $\mathbf{x}_k \in \Omega$ and is denoted by $\mathbf{u}_k^h = (\psi_k^h, \varphi_{n;k}^h, \varphi_{p;k}^h) \in \mathbb{R}^3$. If we want to distinguish the different numerical solutions from each other, we drop the superscript h and replace it with the acronym of the corresponding discretization method (FD, FE or FV) to make it clear which one is meant.

3.1 Finite difference method

In one spatial dimension we consider the interval $\Omega = [0, 3L]$ for some $L < 0$ and want to approximate the solution at discrete points $0 = x_1 < \ldots < x_N = 3L$. In particular we seek to approximate $\psi(x_k) \approx \psi_k^h$, $\varphi_n(x_k) \approx \varphi_{n;k}^h$, and $\varphi_p(x_k) \approx \varphi_{p;k}^h$. The standard 3-point finite difference stencil for the elliptic operator $[Au](x) = -\big(a(x)u'(x)\big)'$ is

$$(Au^h)_k = -\frac{1}{h_k}\left[a_{k+1/2}\frac{u_{k+1}^h - u_k^h}{h_{k+1/2}} - a_{k-1/2}\frac{u_k^h - u_{k-1}^h}{h_{k-1/2}}\right], \tag{24}$$

where $h_{k\pm 1/2} = |x_{k\pm 1} - x_k|$ and $h_k = \frac{1}{2}|x_{k+1} - x_{k-1}|$. The discretization of the Poisson equation (1a) uses a spatially constant $a = \varepsilon_0\varepsilon_r$, whereas in the discretization of the transport equation for the electron current we use $a_{k+1/2} = \frac{1}{2}q\mu_n(n_k^h + n_{k+1}^h)$, where $n_k^h = n\big(\eta_n(\mathbf{u}_k^h)\big)$ is the electron density computed from the discrete potentials $\mathbf{u}_k^h$ using the equation of state (2). With vanishing recombination the total current $I = L^2(I_n + I_p)$ is computed from averages of the constant local current density via $I_n = -\frac{1}{3L}\int_0^{3L} q\mu_n n\varphi_n' \mathrm{d}x$ and $I_p = -\frac{1}{3L}\int_0^{3L} q\mu_p p\varphi_p' \mathrm{d}x$. Using a trapezoidal rule its discrete approximation is

$$I_n^h = -\frac{1}{3L}\sum_{k=1}^{N-1} q\mu_n(x_{k+1} - x_k)\frac{(n_k^h + n_{k+1}^h)}{2}\frac{\varphi_{n;k+1}^h - \varphi_{n;k}^h}{x_{k+1} - x_k}, \tag{25a}$$

$$I_p^h = -\frac{1}{3L}\sum_{k=1}^{N-1} q\mu_p(x_{i+1} - x_i)\frac{(p_k^h + p_{k+1}^h)}{2}\frac{\varphi_{p;k+1}^h - \varphi_{p;k}^h}{x_{k+1} - x_k}, \tag{25b}$$

which we will later see can be beneficial for its convergence order. The purpose of the factor L^2 is that we end up with actual currents in Ampere and current densities in Ampere per area, so that one can

compare 1D and 2D simulations appropriately. A similar strategy will be used to evaluate the currents for the finite element method.

3.2 Finite element method

Assume $\Omega \subset \mathbb{R}^2$ is a polygonal domain and let $\mathcal{T}_h$ be an admissible decomposition of Ω into N_{tria} triangles and N_{vert} vertices, such that $\Omega = \bigcup_{t=1}^{N_{\text{tria}}} \tau_t$ for $\tau_t \in \mathcal{T}_h$ as for example shown in Figure 1. Similar as in [2], we solve the stationary van Roosbroeck system (1) using a standard P_1 finite element method. We seek the electrostatic potential and the quasi-Fermi potentials $\mathbf{u}^h = (\psi^h, \varphi_n^h, \varphi_p^h) \in V^h$, such that the van Roosbroeck system can be written in the weak form as

$$0 = \int_\Omega \varepsilon_0 \varepsilon_r \nabla \psi^h \cdot \nabla v_i - q\big(C + p^h - n^h\big) v_i \,\mathrm{d}x, \tag{26a}$$

$$0 = \int_\Omega q\mu_n n^h \nabla \varphi_n^h \cdot \nabla v_j - qR(n^h, p^h) v_j \,\mathrm{d}x, \tag{26b}$$

$$0 = \int_\Omega q\mu_p p^h \nabla \varphi_p^h \cdot \nabla v_k + qR(n^h, p^h) v_k \,\mathrm{d}x, \tag{26c}$$

for all suitable test functions $\mathbf{v}^h = (v_i, v_j, v_k) \in V^h$, where $V^h \cong \mathbb{R}^{N_{\text{vert}} \times 3}$ is the $3N_{\text{vert}}$ dimensional space of vectorial continuous functions which are piecewise linear on each triangle τ_t. The carrier densities $n^h = n\big(\eta_n(\psi^h, \varphi_n^h)\big), p^h = p\big(\eta_p(\psi^h, \varphi_p^h)\big)$ depend explicitly on $\mathbf{u}^h$ via the equation of state (2). The basis functions for the function space V^h are uniquely defined by $v_j(\mathbf{x}_k) = \delta_{jk}$, where j, k run over all N_{vert} indices corresponding to vertices $\mathbf{x}_j, \mathbf{x}_k$ of the triangulation. This allows us to represent a solution of (26) as

$$\psi^h(\mathbf{x}) = \sum_{k=1}^{N_{\text{vert}}} \psi_k^h v_k(\mathbf{x}), \quad \varphi_n^h(\mathbf{x}) = \sum_{k=1}^{N_{\text{vert}}} \varphi_{n;k}^h v_k(\mathbf{x}), \quad \varphi_p^h(\mathbf{x}) = \sum_{k=1}^{N_{\text{vert}}} \varphi_{p;k}^h v_k(\mathbf{x}), \tag{27}$$

which explains the equivalence of functions $\psi^h(\mathbf{x}) \in V^h$ and matrices $\psi^h \in \mathbb{R}^{N_{\text{vert}} \times 3}$. Some integrals in (26) can be evaluated exactly, the remaining integrals are computed using a standard 7-point Gauss quadrature for triangles [11]. At Ohmic contacts Γ_D we impose inhomogeneous Dirichlet boundary

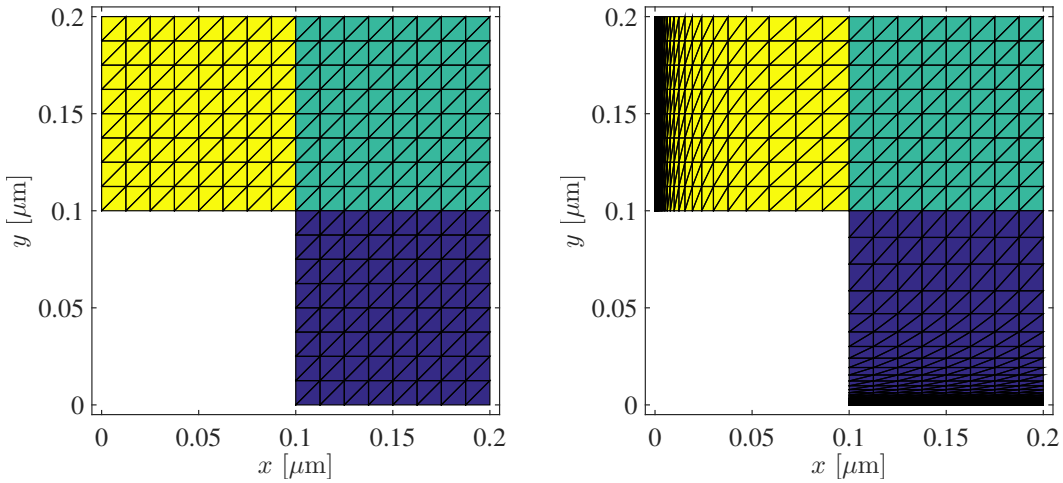

Figure 1: Domain and mesh with $h \sim 2^{-3}$ (left) uniform and (right) boundary adapted.

conditions $\mathbf{u}_D$ as defined in (6a). We realize them by setting $\mathbf{u} = \tilde{\mathbf{u}} + \mathbf{u}_D$ with $\tilde{\mathbf{u}} = 0$ on Γ_D so that

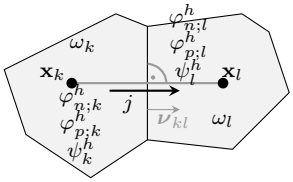

Figure 2: Two adjacent control volumes ω_k and ω_l with corresponding notation.

all essential boundary conditions are automatically satisfied. This reduces the dimension of the discrete problem to N_{vert} only representing vertices not lying on any Γ_α. For a given Ohmic contact α, in order to compute currents, we use an auxiliary function w with $w(\mathbf{x}) = \delta_{\alpha\beta}$ for $\mathbf{x} \in \Gamma_\beta$ and rewrite the current according to

$$\begin{aligned} I_n^\alpha &= \int_{\Gamma_\alpha} \mathbf{j}_n \cdot \boldsymbol{\nu} \,\mathrm{d}a = \int_{\partial\Omega} w\, \mathbf{j}_n \cdot \boldsymbol{\nu} \,\mathrm{d}a = \int_\Omega \nabla \cdot (w \mathbf{j}_n) \,\mathrm{d}\mathbf{x} \\ &= \int_\Omega \nabla w \cdot \mathbf{j}_n + w \nabla \cdot \mathbf{j}_n \,\mathrm{d}\mathbf{x} = -\int_\Omega \left(q\mu_n n \nabla w \cdot \nabla \varphi_n - qwR \right) \mathrm{d}\mathbf{x}, \end{aligned} \tag{28a}$$

and analogously

$$I_p^\alpha = -\int_\Omega \left(q\mu_p p \nabla w \cdot \nabla \varphi_p + qwR \right) \mathrm{d}\mathbf{x}. \tag{28b}$$

Then the total current $I = L(I_n^\alpha + I_p^\alpha)$ can be easily evaluated using the operators from the existing weak form of the van Roosbroeck system (26). Again, the prefactor L ensures that we end up with currents in Ampere. The auxiliary function w is chosen by solving $\Delta w = 0$ with Dirichlet data for w mentioned before and with homogeneous Neumann boundary conditions on Γ, e.g. see [18].

3.3 Finite volume method

In this section, we present a Voronoï finite volume technique [19, 18, 17, 27]. Similar as for finite elements, we start by partitioning the domain Ω into non-intersecting, convex polyhedral control volumes ω_k such that $\Omega = \bigcup_{k=1}^{N_{\text{vert}}} \omega_k$. Unlike for finite elements, these control volumes need not to be triangular but fulfill the following orthogonality condition: We associate with each control volume ω_k a node $\mathbf{x}_k \in \omega_k$. For every boundary intersecting control volume, we demand that this node lies on the boundary $\mathbf{x}_k \in \partial\Omega \cap \omega_k$. Assuming that the partition is admissible in the sense of [13], that is the edge $\overline{\mathbf{x}_k\mathbf{x}_l}$ of length h_{kl} is orthogonal to $\partial\omega_k \cap \partial\omega_l$, the normal vectors to $\partial\omega_k$ can be calculated by $\boldsymbol{\nu}_{kl} = (\mathbf{x}_l - \mathbf{x}_k)/\|\mathbf{x}_l - \mathbf{x}_k\|$. The notation is explained visually in Figure 2.

For each control volume ω_k, the finite volume discretization is given by the three equations:

$$\sum_{\omega_l \in \mathcal{N}(\omega_k)} |\partial\omega_k \cap \partial\omega_l| j_{\psi;k,l} = q|\omega_k| \left(C_k + p_k^h - n_k^h \right), \tag{29a}$$

$$\sum_{\omega_l \in \mathcal{N}(\omega_k)} |\partial\omega_k \cap \partial\omega_l| j_{n;k,l} = +q|\omega_k| R_k, \tag{29b}$$

$$\sum_{\omega_l \in \mathcal{N}(\omega_k)} |\partial\omega_k \cap \partial\omega_l| j_{p;k,l} = -q|\omega_k| R_k. \tag{29c}$$

We denote with $\mathcal{N}(\omega_k)$ the set of all control volumes neighboring ω_k. In 2D, the measure $|\partial\omega_k \cap \partial\omega_l|$ corresponds to the length of the boundary line segment and in 3D to the area of the intersection of the

boundary surfaces. Furthermore, in 2D the measure $|\omega_k|$ is given by the area and in 3D by the volume of the control volume ω_k. The unknowns ψ_k^h, $\varphi_{n;k}^h$ correspond to the electrostatic potential as well as the quasi Fermi potentials for electrons and holes evaluated at node $\mathbf{x}_k$. Accordingly, n_k^h, p_k^h, R_k and C_k are defined as

$$n_k^h = N_c \mathcal{F}\big(\eta_n(\psi_k^h, \varphi_{n;k}^h)\big), \qquad C_k = C(\mathbf{x}_k), \tag{30a}$$

$$p_k^h = N_v \mathcal{F}\big(\eta_p(\psi_k^h, \varphi_{p;k}^h)\big), \qquad R_k = R\big(n_k^h, p_k^h\big). \tag{30b}$$

Note that the doping profile C and the recombination rate R are known a priori. The numerical fluxes $j_{\psi;k,l}$, $j_{n;k,l}$ and $j_{p;k,l}$ approximate respectively $-\varepsilon_0\varepsilon_r \nabla\psi \cdot \boldsymbol{\nu}_{kl}$, $\mathbf{j}_n \cdot \boldsymbol{\nu}_{kl}$ and $\mathbf{j}_p \cdot \boldsymbol{\nu}_{kl}$ on the interfaces between two adjacent control volumes ω_k and ω_l. These fluxes can be expressed as functions depending nonlinearly on the values $\psi_k^h, \varphi_{n;k}^h, \varphi_{p;k}^h$ and $\psi_l^h, \varphi_{n;l}^h, \varphi_{p;l}^h$. The flux corresponding to the electrostatic displacement is approximated by

$$j_{\psi;k,l} = -\varepsilon_0\varepsilon_r \frac{\psi_l^h - \psi_k^h}{\|\mathbf{x}_l - \mathbf{x}_k\|}.$$

The numerical flux approximations for the continuity fluxes we discuss next.

3.3.1 Flux discretizations for Boltzmann statistics

Choosing the numerical fluxes $j_{n;k,l}$ and $j_{p;k,l}$ correctly is a rather delicate issue as the wrong choice may lead to either instabilities or the violation of thermodynamic principles. Scharfetter and Gummel presented in [26] a suitable choice for Boltzmann statistics. It is possible to derive it from the local one-dimensional homogeneous boundary value problem

$$\partial_x \left(D_n \partial_x n - v n\right) = 0 \quad \text{with } n(x_k) = n_k \text{ and } n(x_l) = n_l$$

with the linear diffusion constant $D_n = \mu_n U_T$ and the velocity $v = \mu_n \frac{\psi_l^h - \psi_k^h}{x_l - x_k}$, assuming that the electrostatic potential can be resolved with a linear function. We point out once more that the choice for the diffusion constant implies that we are in the Boltzmann regime. The above differential equation is structurally the same as the leading-order equation (20). Since it is homogeneous, it can be interpreted as demanding that the electron flux is constant. The solution to this boundary value problem is readily verified to be

$$n(x) = n_l \frac{1 - e^{\frac{v}{D_n}(x - x_k)}}{1 - e^{\frac{v}{D_n}(x_l - x_k)}} + n_k \frac{e^{\frac{v}{D_n}(x - x_k)} - e^{\frac{v}{D_n}(x_l - x_k)}}{1 - e^{\frac{v}{D_n}(x_l - x_k)}}.$$

Thus the constant Scharfetter-Gummel flux is given by

$$j_{n;k,l} = -\frac{q\mu_n N_c U_T}{x_l - x_k} \left(\exp\left(\eta_{n;k}^h\right) B\left(-\frac{\psi_l^h - \psi_k^h}{U_T}\right) - \exp\left(\eta_{n;l}^h\right) B\left(\frac{\psi_l^h - \psi_k^h}{U_T}\right) \right) \tag{31}$$

with $\eta_{n;k}^h = \eta_n(\psi_k^h, \varphi_{n;k}^h)$ and $\eta_{n;l}^h = \eta_n(\psi_l^h, \varphi_{n;l}^h)$. A similar expression can be derived for the hole flux. We point out that only in the Boltzmann regime this flux is thermodynamically consistent in the sense that constant quasi Fermi potentials imply that the flux vanishes.

Finally, we wish to reinterpret the width of the boundary layer from Section 2 in terms of numerical quantities. Making use of the Boltzmann assumption, we invert (2) for the quasi Fermi potential to obtain

$$\varphi_n(x) = \psi(x) - U_T \log\left(\frac{n(x)}{N_c}\right) - \frac{E_c}{q}. \tag{32}$$

Now we use the expansions

$$n(x) \approx \frac{n_l^h - n_k^h}{x_l - x_k}(x - x_k) + n_k^h, \qquad \psi(x) \approx \frac{\psi_l^h - \psi_k^h}{x_l - x_k}(x - x_k) + \psi_k^h, \tag{33}$$

where n_l^h, n_k^h and ψ_l^h, ψ_k^h denote the numerical solution of the electron density and the electrostatic potential at nodes x_l and x_k. Assuming that the Ohmic contact is located at x_k, we can derive a considerably simpler approximation for the quasi Fermi potential by expanding (32) around $x \approx x_k$

$$\varphi_n(x) \approx \psi(x) - U_T \log\left(\frac{x - x_k + \ell_J^h}{\ell_J^h}\right) - U_T \log\left(\frac{n_k^h}{N_c}\right) - \frac{E_c}{q}, \tag{34}$$

very similar to (22) and where

$$\ell_J^h = n_k^h \left(\frac{x_l - x_k}{n_l^h - n_k^h}\right) \approx \left.\frac{n}{n'}\right|_{x=x_k} \approx \frac{q\mu_n n_k U_T}{J} = \ell_J$$

denotes the approximative boundary layer width, an approximation of the previously derived boundary layer width (14). In particular, $\ell_J^h \to \ell_J$ for $h = |x_l - x_k| \to 0$. The approximations follow from the observation that in our setting

$$n' = \frac{q}{k_B T} n(\psi' - \varphi_n') \approx -\frac{q}{k_B T} n \varphi_n' = \frac{J}{\mu_n k_B T}.$$

We can also approximate the derivative of φ_n by differentiating (34) and obtain

$$\varphi_n'(x) \approx \frac{\psi_l^h - \psi_k^h}{x_l - x_k} - U_T \frac{1}{x + \ell_J^h}. \tag{35}$$

3.3.2 Flux discretization for general statistics

For general statistics functions $\mathcal{F}$, ideas from Bessemoulin-Chatard [7] are useful to derive a finite volume scheme for convection-diffusion problems in a thermodynamically consistent way by averaging the nonlinear diffusion term appropriately. In [21], the nonlinear diffusion was expressed via a logarithmic average of the nonlinear diffusion enhancement

$$g_{kl} = \frac{\eta_{n;l}^h - \eta_{n;k}^h}{\log \mathcal{F}\left(\eta_{n;l}^h\right) - \log \mathcal{F}\left(\eta_{n;k}^h\right)} \tag{36}$$

along the discretization edge. Using the generalized Einstein relation (5a), one immediately observes that the diffusion enhancement g can be seen as a modification factor for the thermal voltage U_T. Replacing U_T in the original expression (31) by $U_T^* = U_T g_{kl}$, we deduce the following modified Scharfetter-Gummel scheme

$$j_{n;k,l} = -\frac{q\mu_n N_c U_T}{x_l - x_k} g_{kl} \left(\mathcal{F}\left(\eta_{n;k}^h\right) B\left(-\frac{\psi_l^h - \psi_k^h}{U_T g_{kl}}\right) - \mathcal{F}\left(\eta_{n;l}^h\right) B\left(\frac{\psi_l^h - \psi_k^h}{U_T g_{kl}}\right)\right), \tag{37}$$

approximating the (electron) current along the edge. Again a similar expression can be derived for the hole flux. A problematic aspect of this scheme is that even though the diffusion enhancement factor g_{kl} is bounded from below by one, it is not straightforward to compute it on a computer when $\eta_{n;k}^h$ approaches $\eta_{n;l}^h$. In this case one needs to use a suitable regularization strategy.

4 Numerical comparisons in 1D

In this section, we are going to present numerical solutions of the van Roosbroeck system via FE/FD and the Scharfetter-Gummel FV discretization. In one dimension we focus on two challenges, which have an impact on the convergence rate of solutions: the size of a boundary layer and the regularity of the doping. Since in this section we are mostly concerned with numerical solutions, we will drop the superindex h. If necessary, we replace it with the acronym of the corresponding discretization method. Also we remind the reader that we solve the van Roosbroeck system without recombination, *i.e.*, $R \equiv 0$. Throughout this section, we use the Blakemore distribution function.

As discussed before the solutions develop a boundary layer of thickness ℓ_J, which is minuscule compared to the size of the computational domain $\mathcal{O}(L)$ – it is even several orders of magnitude smaller than the Debye length λ_D. The physical parameter used here (see Section 6) suggest we have

$$\lambda_D = 13.6\,\text{nm}, \qquad J_{\text{lim}} = 1.2 \cdot 10^{-18}\,\text{kA/cm}^2$$

so that $\ell_J = (J_{\text{lim}}/J)\,\lambda_D$ is much smaller than the Debye length for typical currents J. Thus, it is both physically questionable and numerically hopeless to resolve this length scale explicitly when $J \gg J_{\text{lim}}$. As we have seen in Table 1 for typical semiconductor materials the limiting currents are surprisingly low. Hence, it is likely that boundary layers appear.

Moreover, we are going to highlight the impact of the regularity of the doping on the convergence order of the solutions by comparing smooth and quasi-discontinuous doping profiles. For this purpose, we consider the doping $C\colon \Omega \to \mathbb{R}$ on the domain $\Omega = [0, 3L]$ with $L = 10^{-7}$m given by

$$C(x) = \frac{C_0}{2}\Big[1 + \tanh\big(\kappa(0.1 - x[\mu m])\big) - \big\{1 + \tanh\big(\kappa(x[\mu m] - 0.2)\big)\big\}\Big] \tag{38}$$

with Ohmic contacts at $x = 0$ and $x = 3L$. Two cases $\kappa = 500$ and $\kappa = 5 \cdot 10^5$ will be studied. Only the first case leads to a doping in which the jumps are resolved by our sequence of meshes

$$h = 3L \cdot 2^{-M} \qquad \text{for} \qquad M = 1, \dots, 14. \tag{39}$$

The prefactor is set to $C_0 = 10^{23}\text{m}^{-3}$ and constitutes also the largest doping value $C_{\text{m}} = C_0$. The bias is in the range $V_{\text{ext}} \in [0, 3V]$. Hence, as long as $h > L/\kappa$ one will observe an apparent jump discontinuity in the doping C with a direct impact on the convergence rates.

4.1 Resolution of boundary layer

In Figure 3 the electron and hole densities n, p and the doping C are shown for the two cases $\kappa = 5 \cdot 10^2$ and $\kappa = 5 \cdot 10^5$ at $V_{\text{ext}} = 3V$. Note that in both cases, the hole density p has a boundary layer at $x = 0$ and the electron density n has a boundary layer at $x = 0.3\mu m$. This boundary layer, however, is on the length scale of λ_D and therefore nicely resolved by the mesh. On the level of the plot, the difference between the two alternative doping profiles is not visible.

In the left panel of Figure 4 we show the equilibrium electrostatic potential ψ, whereas in the right panel the potentials $(\varphi_n, \varphi_p, \psi)$ for $V_{\text{ext}} = 3V$ are shown. While the electrostatic potential in both cases is a rather smooth function (see right panel of Figure 4), the quasi-Fermi potentials have a boundary layer of size ℓ_J that can not be resolved on any of the meshes (39). This logarithmic boundary layer is predicted by our analysis in Section 2.

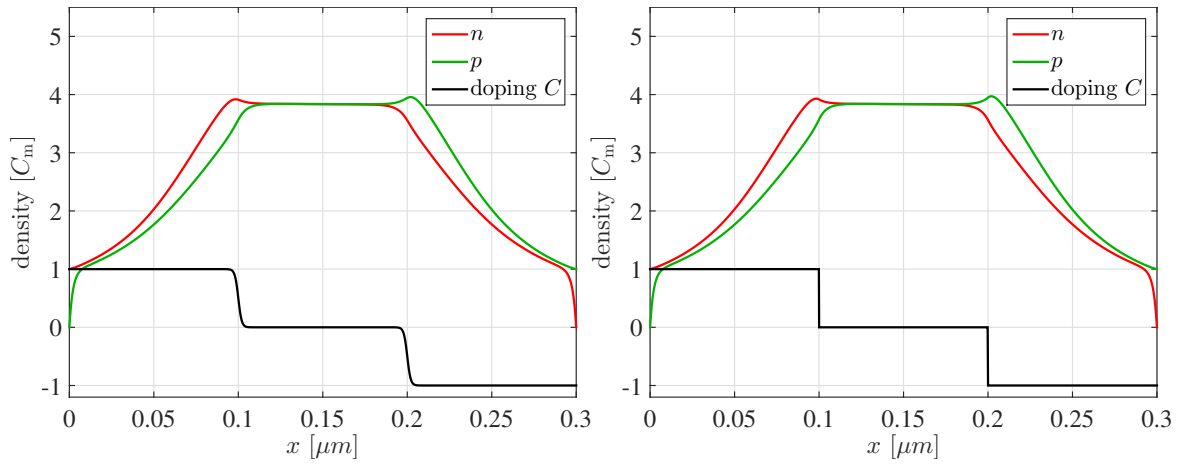

Figure 3: Electron and hole densities n, p and doping C at bias $V_{\text{ext}} = 3V$ shown (left) with $\kappa = 500$ and (right) with $\kappa = 5 \cdot 10^5$, the former yielding a smooth doping profile and the latter practically a discontinuous one.

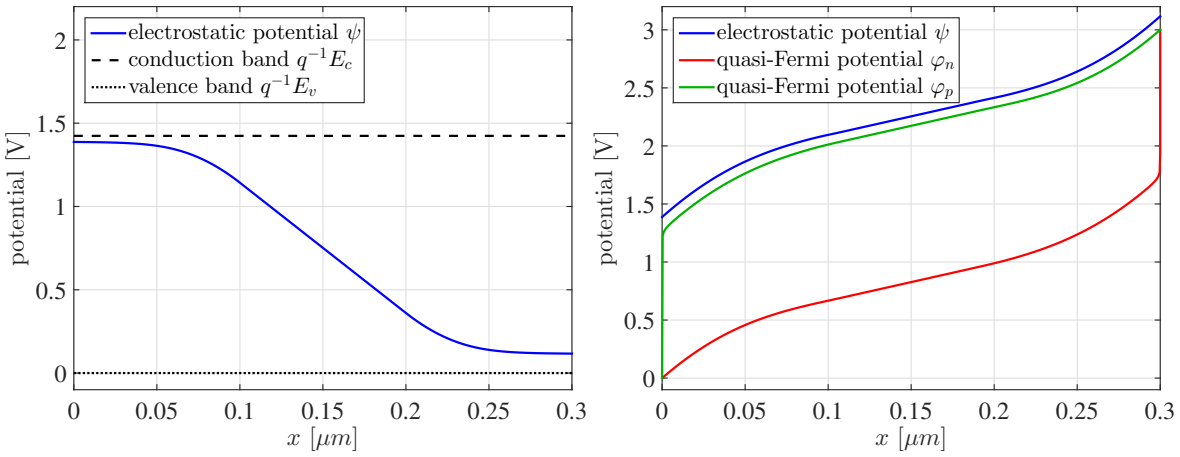

Figure 4: Quasi-Fermi potentials of electrons and holes φ_n, φ_p and electrostatic potential ψ shown (left) in thermal equilibrium $V_{\text{ext}} = 0$ with $\varphi_n = \varphi_p = 0$ and (right) with bias $V_{\text{ext}} = 3V$.

As one can see in Figure 5, the solution effectively jumps within the last interval before the Ohmic contact. An important first observation is that already for moderate mesh sizes the FV quasi-Fermi potentials agree on coarse meshes relatively well with quasi-Fermi potentials on the finest mesh. This implies that, already on meshes which massively undersample the boundary layer width ℓ_J, the FV solution quite accurately agrees with the asymptotic logarithmic solution, see (22). The FD convergence is considerably slower near the Ohmic contact. In particular, on the last few intervals the FD approximation considerably deviates from the asymptotic solution.

In order to analyze the behavior near Ohmic contacts, in the left panel of Figure 6 we compare the electron quasi-Fermi potential φ_n from the FV and FD solution on the finest mesh with the asymptotic solution from (22) on a semi-logarithmic scale. The figure depicts three different regions shown by the shaded areas. The rightmost shaded area (red) is the outer region where $x \sim \lambda_D$, which we are able resolve using our discrete meshes (39). Then there is a wide transient zone $0 < \ell_J \ll x \ll \lambda_D \ll L$ (green), where the quasi-Fermi potential has a logarithmic singularity. We can see that the FD scheme deviates from the predicted boundary layer asymptotic on the last few grid points, as we already observed in the discussion of Figure 5.

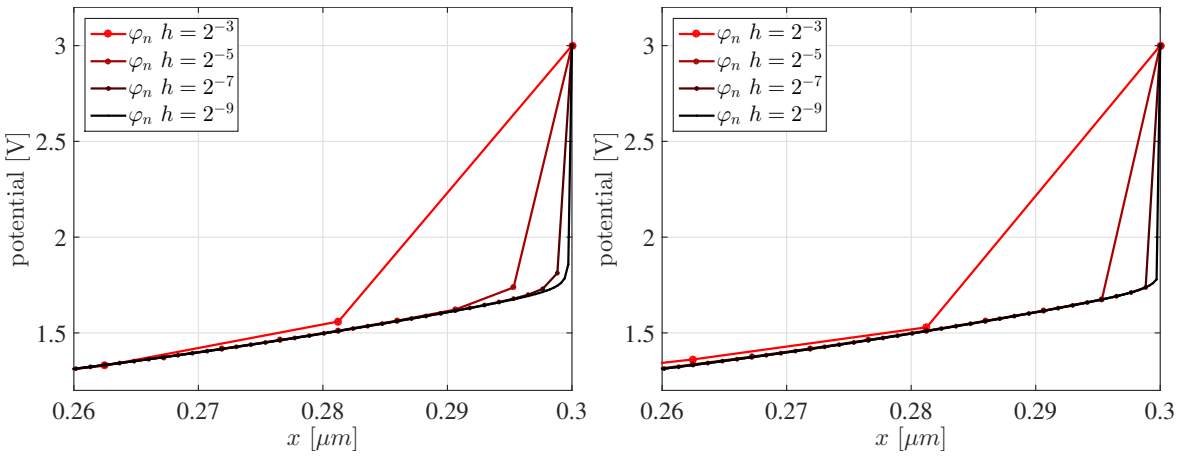

Figure 5: Boundary layers in the electron quasi-Fermi potential φ_n near $x = 0.3\mu m$ for different mesh resolutions h (left) for finite difference and (right) Scharfetter-Gummel type finite volume discretization for $\kappa = 500$.

This singularity is only resolved when $x \sim \ell_J$, where φ_n attains the value set by the Dirichlet boundary condition of the Ohmic contact. Note, that for $V_{\text{ext}} = 3V$ the width of the boundary layer is $\ell_J \sim 10^{-30}$m, which is beyond any meaningful physical scale for this problem. However, note that the FV and the FD solution nicely agree and follow the intermediate logarithmic singularity set by the asymptotic analysis.

In order to show ℓ_J as a function of the bias, we plot in the right panel of Figure 6 the ratio J/J_{lim}, from which using (14) and (15) we can deduce $\ell_J(V_{\text{ext}}) = (J_{\text{lim}}/J(V_{\text{ext}}))\lambda_D$. We observe that the current J follows the standard diode characteristic for the current density $J(V_{\text{ext}}) = J_0(\exp(V_{\text{ext}}/U_T) - 1)$ with a fitted value of $J_0 \approx 0.3J_{\text{lim}}$. This gives us the following expression for the boundary layer thickness:

$$\ell_J \approx \frac{\lambda_D}{0.3(\exp(V_{\text{ext}}/U_T) - 1)}. \tag{40}$$

For instance, for $V_{\text{ext}} = 0.2$V we have a moderately small layer width $\ell_J \approx 2 \cdot 10^{-3}\lambda_D$, but for $V_{\text{ext}} = 1$V an unphysically small layer width $\ell_J \approx 5 \cdot 10^{-16}\lambda_D$.

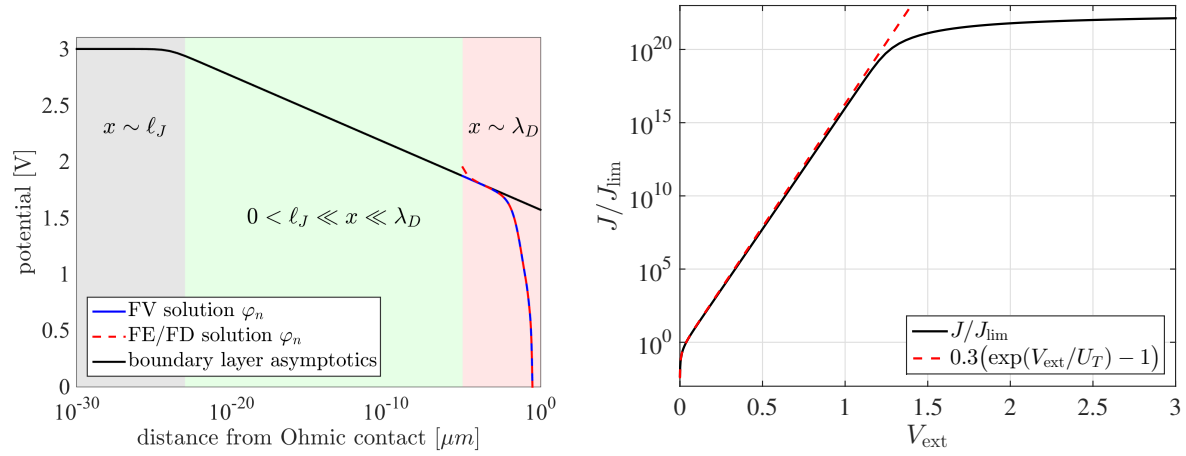

Figure 6: (left) Electron quasi-Fermi potential φ_n from FD and FV solution compared to the boundary layer asymptotics for $V_{\text{ext}} = 3V$ with boundary layer width $\ell_J \sim 10^{-30}m$ and (right) ratio of electron current $J = j_n$ and threshold current J_{lim} gives $\ell_J(V_{\text{ext}}) = (J_{\text{lim}}/J(V_{\text{ext}}))\lambda_D$ as a function of the bias.

4.2 Regularity of the doping

Next, we discuss the influence of the smoothness of the doping on the convergence order for the different discretization methods. Whenever we compare a coarse discrete solution to a finer one, we restrict the finer solution to the coarser mesh. In the left panel of Figure 7 we show the current as a

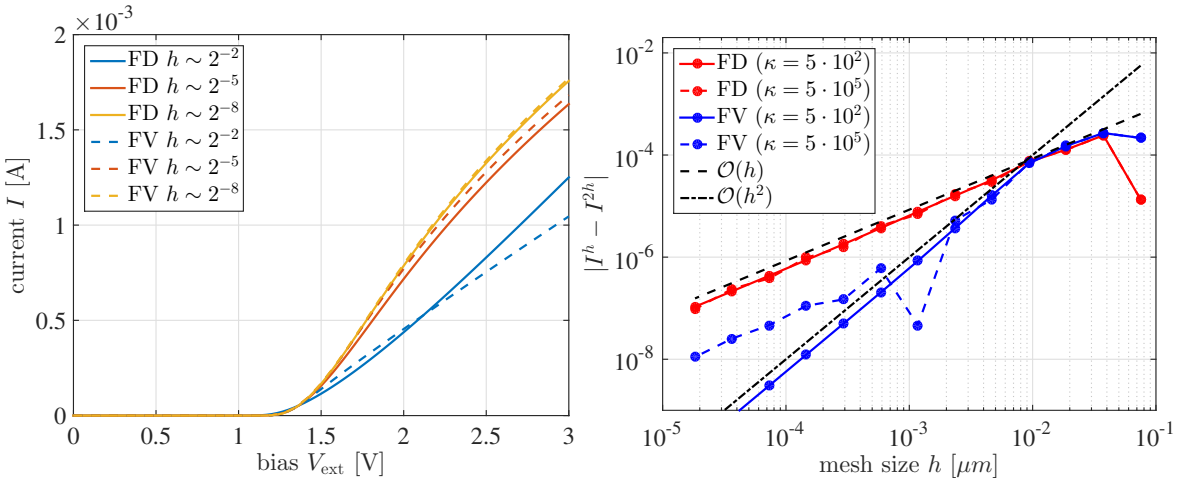

Figure 7: For different mesh sizes h (left) total current J for FD and FV discretization for $\kappa = 500$ and (right) corresponding convergence rates for $\kappa = 5 \cdot 10^2$ and $\kappa = 5 \cdot 10^5$

function of the bias V_{ext} for the FV and FD methods on different meshes for the levels $M = 2, 5, 8$. This already indicates the tendency of the FV method to deliver more accurate solutions on coarser meshes, which is due to the more advanced flux discretization. This becomes even more obvious when comparing the convergence orders for $|I^h - I^{2h}|$ in the right panel of Figure 7. For the smooth doping with $\kappa = 5 \cdot 10^2$ the FV method has a quadratic convergence $|I^h - I^{2h}| \sim h^2$. This order is influenced by the convergence order of the electrostatic potential and the flux. If the Boltzmann approximation is valid and the electrostatic potential linear, then the flux would be nodally exact. Provided that the doping is sufficiently smooth and the carrier densities converge sufficiently fast, then both FD and FV discretization of the Poisson equation are second order schemes, see the convergence for n, p, ψ in the right panel of Figure 8 and the left panel of Figure 9. For the FD method this argument fails, since the quasi-Fermi potentials only converge with order $1/2$ but the densities converge linearly. However, due to the averaging involved in the computation of the current in (28), the convergence order of the FD method in the right panel of Figure 7 is at least linear.

When the doping is discontinuous ($\kappa = 5 \cdot 10^5$), the bottom row in Figure 8 shows that also the convergence order of the FV electrostatic potential becomes linear, which is expected by standard FE error estimates. The dashed lines in the right panel of Figure 7 show that the error for the FD method is still dominated by the error of the quasi-Fermi potentials and densities, whereas the linear convergence of the FV electrostatic potential now also seems to lead to a linear convergence of the FV current.

Interestingly, Figure 9 shows the FV method also allows to evaluate the convergence in the L_∞ norm for $\kappa = 500$. Even though the L_2 error of the solution converges quadratically, one can observe that first the L_∞ error of φ_n and later of φ_p converge linearly. This is due to the flux approximation scheme being first order consistent in the quasi-Fermi potentials near an Ohmic contact with logarithmic singularity. Note, if we had chosen to compute the L_∞ error interpolating the coarser solution to the finer one, we would see no convergence with respect to the grid size defined as in (39).

Even though it appears that the FD scheme cannot compete with the FV method, it is easy to improve

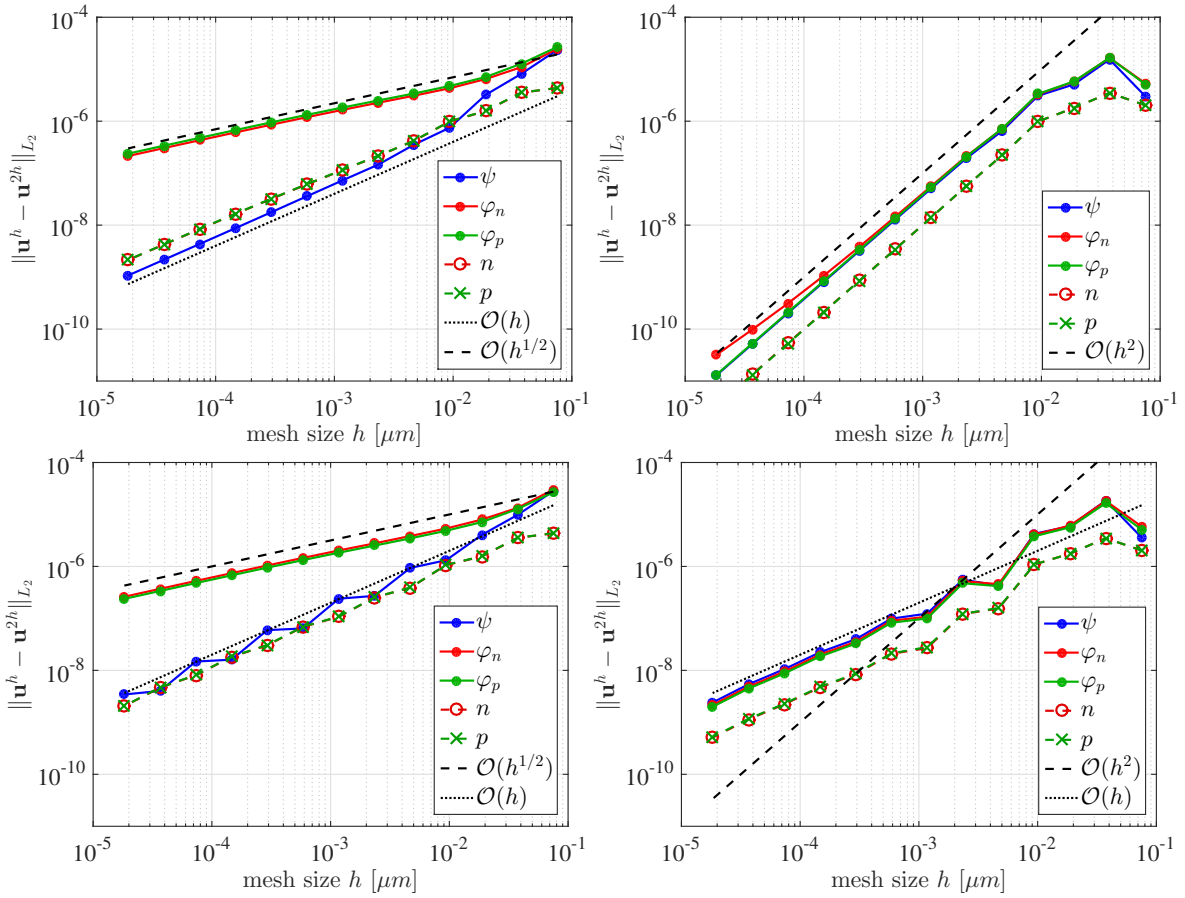

Figure 8: L_2 convergence rates for solution (left) of the FD discretization and (right) of the FV discretization with $\kappa = 500$ in the top row and for $\kappa = 5 \cdot 10^5$ in the bottom row.

it by using boundary-adapted grids as demonstrated in Figure 10. This leads us naturally to our next section, where we study the impact of boundary layers and corner singularities in two spatial dimensions. As boundary layers pose a serious problem for the FD/FE already in one dimension, we are going to compare solutions computed on uniform meshes with those from boundary adapted meshes. However, we will not employ any local refinement strategy near the corner singularity.

5 Numerical comparisons in 2D

5.1 Corner singularities and boundary adapted meshes

Semiconductor devices may often be angular-shaped. However, in particular L-shaped domains pose numerical difficulties which we would like to study for the FE and FV methods.

We consider a two-dimensional L-shaped domain

$$\Omega = [0, 2L]^2 \setminus [0, L]^2 \subset \mathbb{R}^2 \tag{41}$$

as shown in Figure 1 and impose Ohmic contacts at the boundaries $(x, 0)$ and $(0, y)$ for $L \leq x, y \leq 2L$. All other boundaries are supplied with homogeneous Neumann boundary conditions. The p-i-n

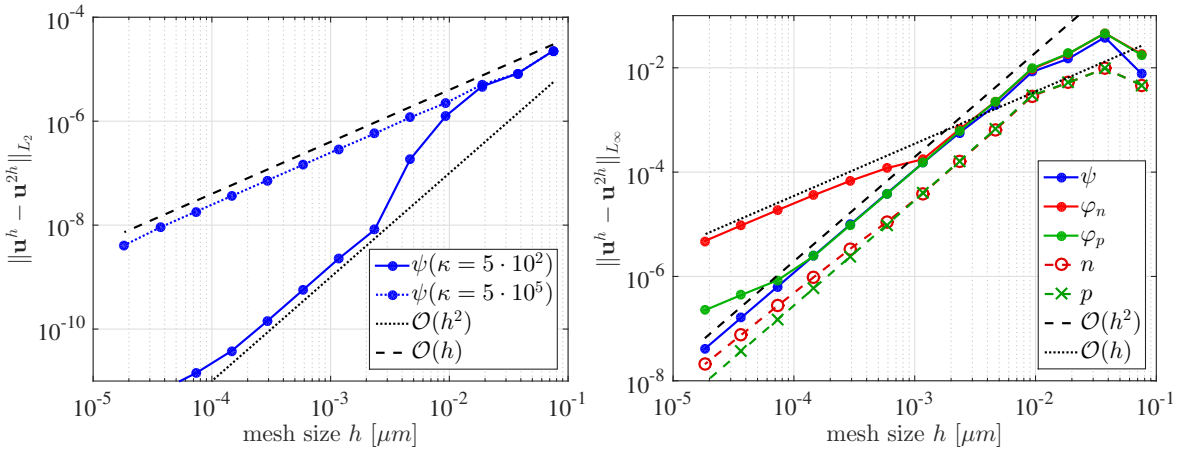

Figure 9: (left) L_2 convergence of ψ in thermal equilibrium (similar for FV and FD) and (right) L_∞ convergence of FV solution at $V_{\text{ext}} = 3V$ for $\kappa = 500$.

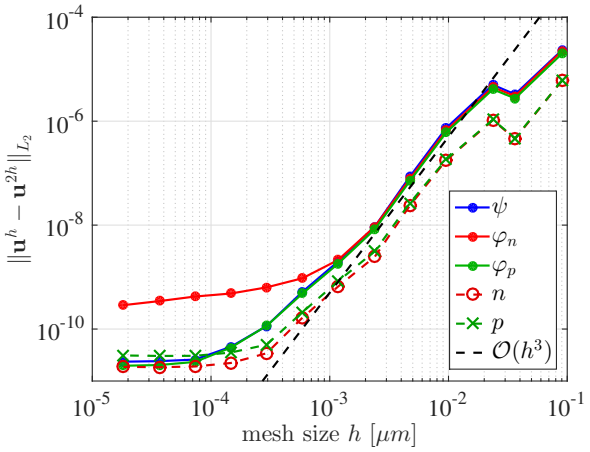

Figure 10: L_2 convergence rates for FD discretization on a non-uniform grid with $\kappa = 500$.

doping concentration $C\colon \Omega \to \mathbb{R}$ is given by

$$C(\mathbf{x}) = \begin{cases} +C_0 & 0 \le x \le L/2, \\ -C_0 & 0 \le y \le L/2, \\ +2C_0(L-x)/L & L/2 < x \le L, \\ -2C_0(L-y)/L & L/2 < y \le L, \\ 0 & \text{otherwise} \end{cases} \tag{42}$$

with $\mathbf{x} = (x, y)$ and as before $L = 10^{-7}m = 0.1\mu$m and $C_0 = C_{\mathsf{m}} = 10^{23}\,\mathrm{m}^{-3}$, see left panel of Figure 11. With this choice we ensure that the convergence order does not suffer from the regularity of the doping. However, constructing a non-convex domain with a corner angle $\vartheta = \theta\pi$ and $\theta = 3/2$ imposes a corner singularity of the form $\psi(\mathbf{x}) \sim r^{1/\theta}$ as $r \to 0$ for $r = \sqrt{(x-x_0)^2 + (y-y_0)^2}$ at $x_0 = y_0 = 0.1\mu m$. Standard finite element error analysis gives $u \in H^\sigma$ with $\sigma = 1 + 1/\theta - \epsilon < 2$ for arbitrary small $\epsilon > 0$, so that

$$\|u - u^h\|_{L_2} \le C\left(h^{l+\sigma-1} + h^{2k}\right)\|u\|_{H^{l+1}}, \qquad l = \min\{k, \sigma - 1\}, \tag{43}$$

where k the polynomial degree of the FE basis functions [28] used to expand u^h. For linear finite elements we obtain the estimate $\|u - u^h\|_{L_2} \le Ch^{4/3-2\epsilon}\|u\|_{H^{5/3-\epsilon}}$, so that the potentials should

converge asymptotically not better than $h^{4/3}$ in the L_2 norm. It remains to be seen how the boundary layer behaves for the FE and FV discretization schemes in two spatial dimensions. In addition to the

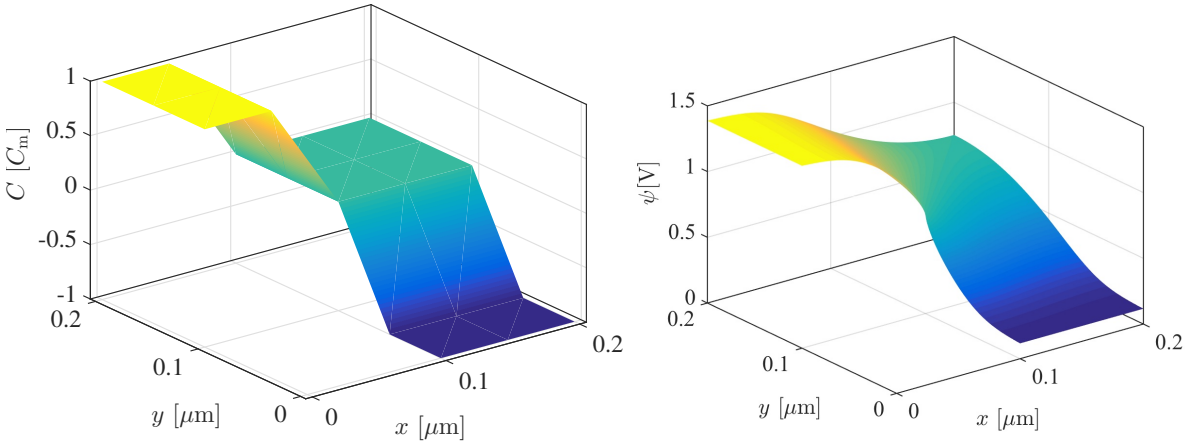

Figure 11: (left) Continuous doping concentration of L-shaped p-i-n diode and (right) electrostatic potential ψ in thermal equilibrium $V_{\text{ext}} = 0$.

series of uniformly refined structured meshes, we are also going to investigate the convergence on meshes adapted to the boundary layers. For a general overview of different strategies for singularly perturbed problems, in particular for boundary adapted meshes, we refer to [25]. The boundary layer is constructed using an exponentially graded mesh, where one direction is kept uniform and towards the Ohmic contact we refine until the shortest triangle edge is approximately $\sim 10^{-5}L$, see right panel in Figure 1.

The electron and hole densities are shown in the upper panels of Figure 12. Similar as in 1D, one can observe boundary layers in n and p, which are well resolved by the mesh and of the order of the Debye length λ_D. However, the lower panels of Figure 12 show the electron and hole quasi-Fermi potentials, which are not resolved and appear to jump on the last row of triangles before one of the Ohmic contacts.

Additionally, in Figure 13 the electrostatic potential and the total current density $\mathbf{j} = \mathbf{j}_n + \mathbf{j}_p$ are shown. A careful inspection of the electrostatic potential and the current density already indicates the presence of the corner singularity. Note, the corner singularity in the total current density $|\mathbf{j}|$ is slightly obscured by the logarithmic scale. The electrostatic potential in thermal equilibrium $V_{\text{ext}} = 0$ is shown in the right panel of Figure 11. A convergence study for this potential should reveal the influence of the corner singularity more clearly, as the transport equations do not interfere here.

For simplicity we will focus here on the discussion of the convergence order for the electrostatic potential ψ and the electron quasi-Fermi potential φ_n. The previous analysis in one dimension should then indicate how the other potential and densities should converge. We focus on the discussion of FE and FV discretizations instead, and also systematically compare uniform and adapted meshes.

The upper left panel of Figure 14 shows the convergence of the electron quasi-Fermi potentials at $V_{\text{ext}} = 3V$, where the FE and FV are compared on a sequence of uniform and a sequence of boundary adapted meshes. As in 1D, the FV method has a quadratic convergence. Furthermore, for the FV discretization the error seems not to be influenced very much by the boundary adapted meshes. In contrast, the FE method again has a lower convergence order and local adaptivity improves the L_2 error of the solution by about one order of magnitude. The upper right panel of Figure 14 shows the convergence of the electrostatic potential at $V_{\text{ext}} = 3V$, for which now the convergence rates are about the same ($\mathcal{O}(h)$) for both schemes and both mesh types. The errors of the FV and FE methods are

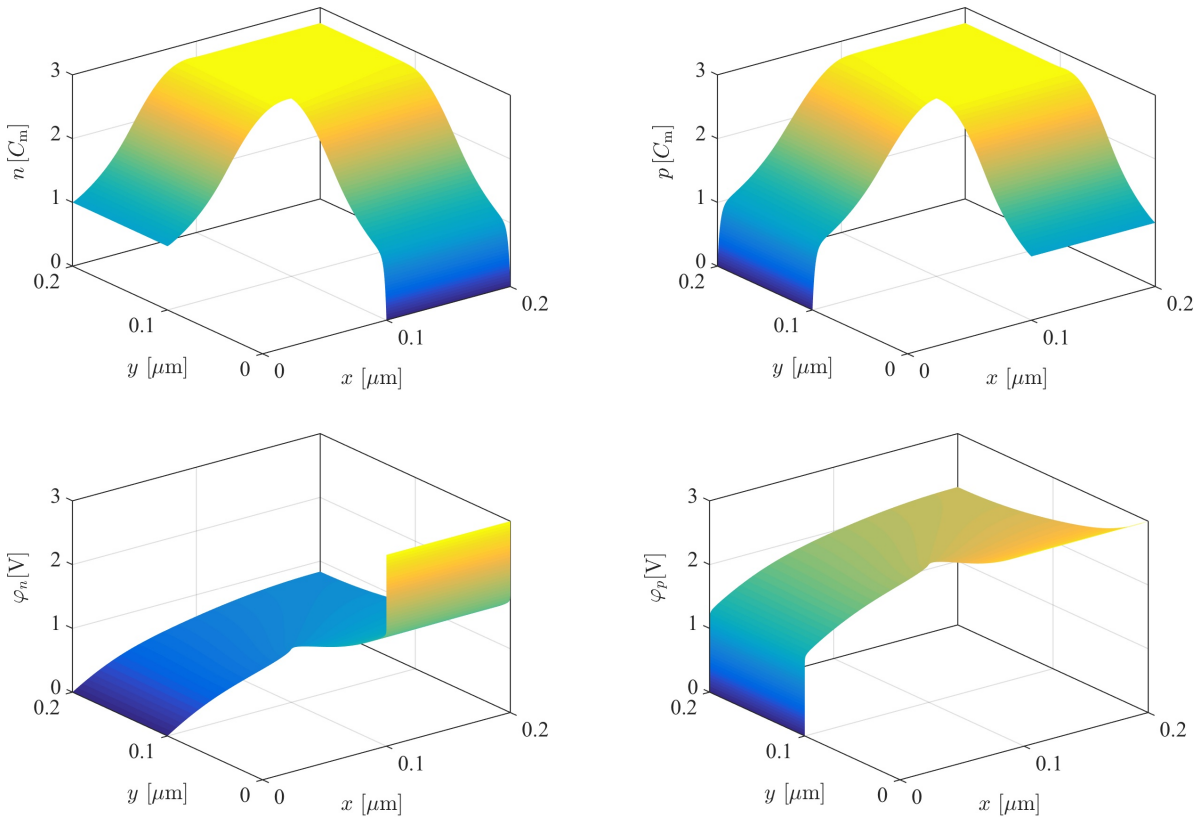

Figure 12: (top, left) Electron density n and (top, right) hole density p and corresponding (bottom, left) electron quasi-Fermi potential φ_n and (bottom, right) hole quasi-Fermi potential φ_p at bias $V_{\text{ext}} = 3\text{V}$.

similar for adaptive and uniformly refined meshes, only the FE with uniform refinement converges slower. It is likely that the more slowly convergent charge density dominates the convergence in this case.

The lower panels of Figure 14 shows the solutions at $V_{\text{ext}} = 0.2V$, where the boundary layer is moderate and solutions are closer to thermal equilibrium. Hence, the lower left panel shows the general tendency to have lower errors. However, the convergence is slower with an order between $\mathcal{O}(h)$ and $\mathcal{O}(h^{4/3})$, indicating a stronger influence of the corner singularity. This effect is even more pronounced in the lower right panel, in which for all the used methods the convergence of the electrostatic potential nicely follows the $\mathcal{O}(h^{4/3})$ order predicted by the error analysis of the corner singularity. The existence of the corner singularity for both bias values becomes obvious by a closer examination of the local error $\mathrm{err}(\mathbf{x}) = |\mathbf{u}^h(\mathbf{x}) - \mathbf{u}^{2h}(\mathbf{x})|$ shown in in Figure 15 on a logarithmic scale. At the Ohmic contacts the error vanishes since the boundary conditions are solved exact. A clearly symmetric and dominant corner singularity is visible in the left panel of Figure 15 for the electrostatic potential at thermal equilibrium. This matches also our previous observation, that the $\mathcal{O}(h^{4/3})$ convergence order is most prominent in the electrostatic potential for low voltages in Figure 14. In a similar manner, we can see that the local error in the middle and right panel of Figure 15 has corner singularities. However, while the local error of the electron quasi-Fermi potential of the FV in the middle panel shows no specific problem near the Ohmic contact, the FE solution also has additional difficulties at the Ohmic contact $y = 0$, where the boundary layer is located, compare with Figure 12.

In Figure 16 the total current for the different methods and the convergence of the total current is shown. Except for the FE method on uniformly refined meshes, all discretization schemes deliver

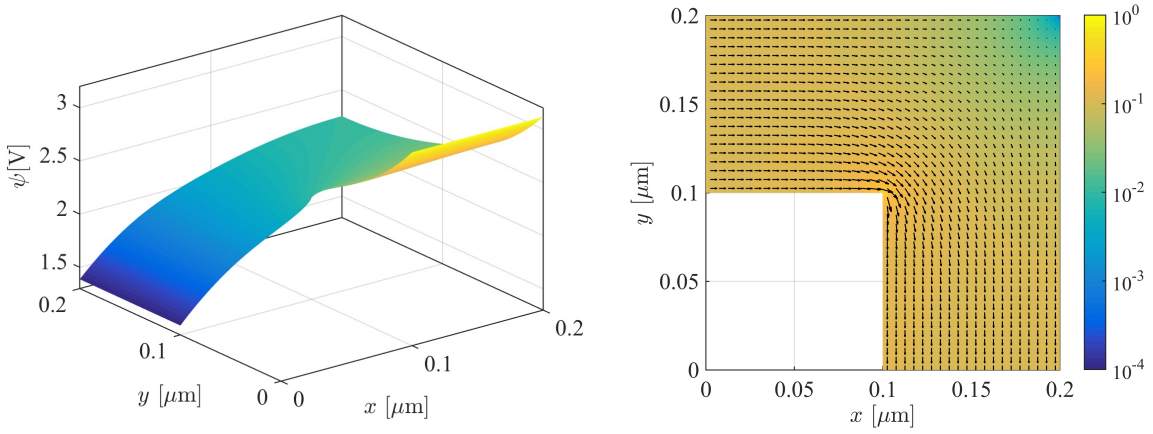

Figure 13: (left) Electrostatic potential ψ at bias $V_{\text{ext}} = 3$V and (right) total current density $\mathbf{j} = \mathbf{j}_n + \mathbf{j}_p$ in arbitrary units.

comparable results, namely a convergence order between $\mathcal{O}(h)$ and $\mathcal{O}(h^2)$. Note that the FE method yields already on the coarsest adaptive mesh ($h \sim 2^{-1}$) with 273 vertices more accurate numerical currents than on the considerably finer uniform mesh ($h \sim 2^{-6}$) with $12\,545$ vertices. However, the FV method does not require boundary adapted meshes, as there is practically no improvement noticeable compared to uniform meshes in the right panel of Figure 16.

Summarizing, in 2D both FE and FV discretizations deliver reasonable results. While the finite volume scheme often shows better convergence rates, the finite element method can be drastically improved by using meshes which are finer near Ohmic contacts. We clearly observe that depending on the potential and the selected bias, the error is dominated by the boundary layer or the corner singularity. While the FV method generally handles the boundary layer well, the FE method in 2D introduces extra oscillations in the boundary layer, see Figure 15.

6 Conclusion

We performed an extensive analysis and comparison of numerical methods for the van Roosbroeck system in one and two spatial dimensions. We compared Scharfetter-Gummel type finite volume discretizations for non-Boltzmann statistics with standard finite element and finite difference methods, where the electrostatic and quasi-Fermi potentials are used as primary variables. This choice of variables transforms the convection-dominated problem into a nearly degenerate elliptic system, making it susceptible for these alternative numerical discretization philosophies. A careful asymptotic analysis showed that the quasi-Fermi potentials corresponding to minority carriers have logarithmic boundary layers at Ohmic contacts. The typical size ℓ_J of these layers depends on the applied voltage via the current density J, *i.e.*, $\ell_J = \lambda_D \, (J_{\text{lim}}/J)$, which due to the smallness of J_{lim} generates layers much thinner than the Debye length for a bias V_{ext} slightly above the thermal voltage U_T. We showed that for $\ell_J \ll x \ll \lambda_D$ the quasi-Fermi potential has a logarithmic singularity.

Nevertheless, all studied methods are able to give reliable predictions for the total electrical current and show the expected convergence behavior in the L_2 norm under mesh refinement. The finite volume approach even converges with respect to the L_∞ norm and generally has the best convergence order among all compared methods.

Already in one dimension, the advantageous convergence order of the finite volume convergence order

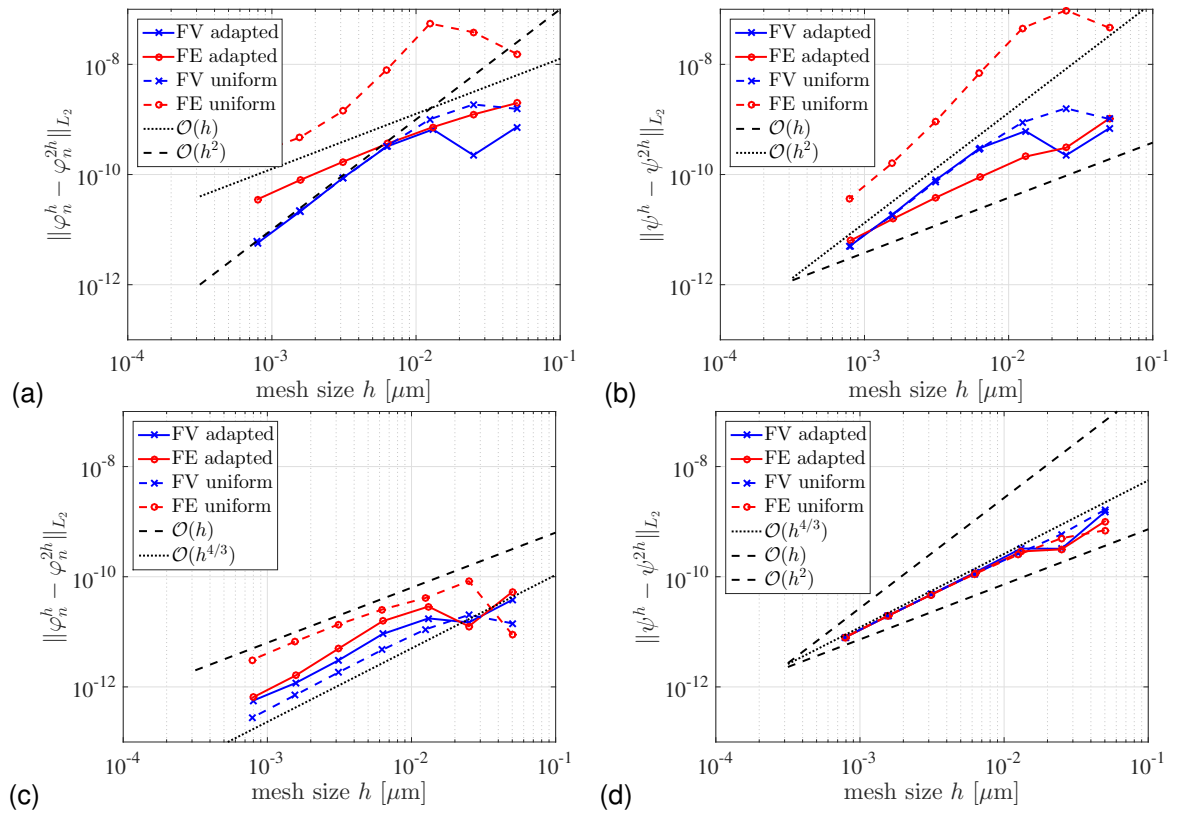

Figure 14: Convergence of solutions on different meshes as a function of relative triangle size $h = 2^{-\ell}$ for (a) electron quasi-Fermi potential φ_n at $V_{\text{ext}} = 3V$, (b) electrostatic potential ψ at $V_{\text{ext}} = 3V$, (c) electron quasi-Fermi potential φ_n at $V_{\text{ext}} = 0.2V$, (d) electrostatic potential ψ at $V_{\text{ext}} = 0.2V$.

is distorted when discontinuous doping profiles are used. However, when used on uniform meshes, the finite volume method usually outperforms the finite element and finite difference approaches significantly. The finite element method can be significantly improved by refining the computational mesh near Ohmic contacts.

In higher dimensions corner singularities can be the ultimate restriction for the convergence order. In practice, their impact is most noticeable at low applied biases. In particular in two dimensions, we have multiple error sources, so that the observed convergence order in the studied range of mesh sizes is not yet in the predicted asymptotic regime dominated by the corner-singularity.

Appendix: material data

Table 6 lists the used material parameters.

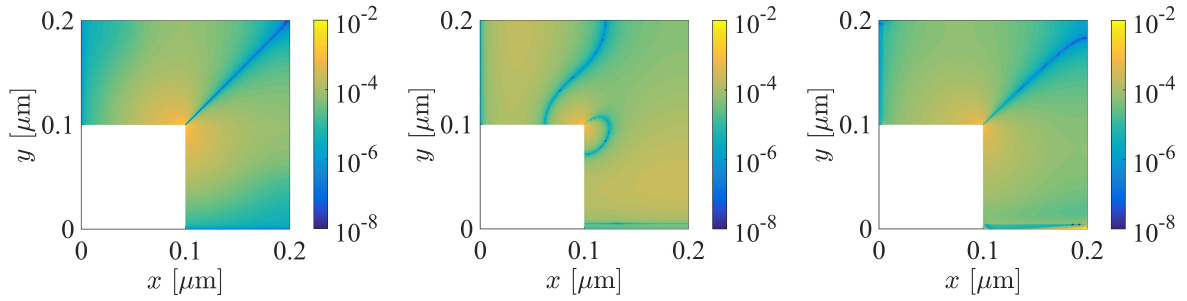

Figure 15: Local errors for (left) electrostatic potential ψ in thermal equilibrium and at $V_{\text{ext}} = 3\text{V}$ for (middle) FV and for (right) FE electron quasi-Fermi potential.

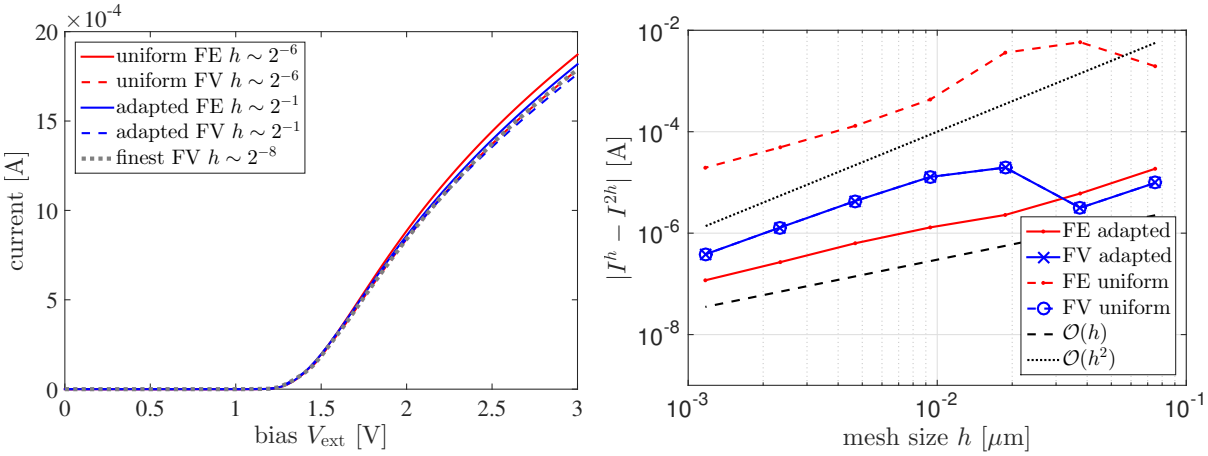

Figure 16: For different mesh sizes h (left) total current I for FE and FV discretizations (right) corresponding convergence rates.

parameter	value	parameter	value
k_{B}	$1.3806503 \cdot 10^{23}$ J/K	ε_{r}	12.9
q	$1.602176565 \cdot 10^{-19}$ C	μ_n	$0.85\,\text{m}^2/\text{Vs}$
μ_p	$0.047\,\text{m}^2/\text{Vs}$	ε_0	$8.854187817 \cdot 10^{-12}$As/Vm
T	300 K	N_c	$4.351959895 \cdot 10^{23}\,\text{m}^{-3}$
N_v	$9.139615903 \cdot 10^{24}\,\text{m}^{-3}$	L	10^{-7}m
C_{m}	10^{23}m^{-3}	E_c	1.424 eV
E_v	0 eV		

Table 2: Material parameters used for the simulations, see also [21].

References

[1] M. Auf der Maur. *A Multiscale Simulation Environment for Electronic and Optoelectronic Devices*. PhD thesis, University of Rom “Tor Vergata”, 2008.

[2] M. Auf der Maur, M. Povolotskyi, F. Sacconi, A. Pecchia, G. Romano, G. Penazzi, and A. Di Carlo. TiberCAD: towards multiscale simulation of optoelectronic devices. *Optical and quantum electronics*, 40(14-15):1077–1083, 2008.

[3] R. E. Bank and D. J. Rose. Some error estimates for the box method. *SIAM J. Numer. Anal*, 24:777–787, 1987.

[4] R. E. Bank, D. J. Rose, and W. Fichtner. Numerical methods for semiconductor device simulation. *SIAM Journal on Scientific and Statistical Computing*, 4(3):416–435, 1983.

[5] A. J. Bard, L. R. Faulkner, J. Leddy, and C. G. Zoski. *Electrochemical methods: fundamentals and applications*, volume 2. Wiley New York, 1980.

[6] J. J. Barnes and R. J. Lomax. Finite-element methods in semiconductor device simulation. *IEEE Transactions on Electron Devices*, 24(8):1082–1089, Aug 1977.

[7] M. Bessemoulin-Chatard. A finite volume scheme for convection–diffusion equations with nonlinear diffusion derived from the Scharfetter–Gummel scheme. *Numerische Mathematik*, 121(4):637–670, 2012.

[8] S. C. Brenner and L. R. Scott. *The Mathematical Theory of Finite Element Methods*, volume 15 of *Texts in Applied Mathematics*. Springer, New York, 3rd edition, 2008.

[9] E. M. Buturla, P. E. Cottrell, B. M. Grossman, and K. A. Salsburg. Finite-element analysis of semiconductor devices: The fielday program. *IBM Journal of Research and Development*, 25(4):218–231, July 1981.

[10] P. Ciarlet. *The Finite Element Method for Elliptic Problems*. SIAM, 2002.

[11] G. Cowper. Gaussian quadrature formulas for triangles. *International Journal for Numerical Methods in Engineering*, 7(3):405–408, 1973.

[12] H. C. Elman, D. J. Silvester, and A. J. Wathen. *Finite Elements and Fast Iterative Solvers: with Applications in Incompressible Fluid Dynamics*. Numerical Mathematics and Scientific Computation. Oxford University Press, Oxford, 2005.

[13] R. Eymard, T. Gallouët, and R. Herbin. Finite volume methods. In *Solution of Equation in $\mathbb{R}^n$ (Part 3), Techniques of Scientific Computing (Part 3)*, volume 7 of *Handbook of Numerical Analysis*, pages 713 – 1018. Elsevier, 2000.

[14] P. Farrell, T. Koprucki, and J. Fuhrmann. Computational and analytical comparison of flux discretizations for the semiconductor device equations beyond Boltzmann statistics. *Journal of Computational Physics*, 346:497–513, 2017.

[15] P. Farrell, M. Patriarca, J. Fuhrmann, and T. Koprucki. Comparison of thermodynamically consistent charge carrier flux discretizations for Fermi-Dirac and Gauss-Fermi statistics. *Optical and Quantum Electronics*, 50(101), 2018.

[16] P. Farrell and D. Peschka. Comparison of different discretization methods for semiconductor drift-diffusion problems - data. http://doi.org/10.20347/WIAS.DATA.3, 2018.

[17] P. Farrell, N. Rotundo, D. H. Doan, M. Kantner, J. Fuhrmann, and T. Koprucki. Mathematical methods: Drift-diffusion models. In J. Piprek, editor, *Handbook of Optoelectronic Device Modeling and Simulation*, chapter 50, pages 733–772. Taylor & Francis, 2017.

[18] H. Gajewski. Analysis und Numerik von Ladungstransport in Halbleitern. *WIAS Report*, (6), 1993. ISSN 0942-9077.

[19] K. Gärtner. Existence of Bounded Discrete Steady-State Solutions of the Van Roosbroeck System on Boundary Conforming Delaunay Grids. *SIAM Journal on Scientific Computing*, 31(2):1347–1362, 2009.

[20] V. John and P. Knobloch. On spurious oscillations at layers diminishing (SOLD) methods for convection–diffusion equations: Part I–A review. *Computer Methods in Applied Mechanics and Engineering*, 196(17):2197–2215, 2007.

[21] T. Koprucki, N. Rotundo, P. Farrell, D. H. Doan, and J. Fuhrmann. On thermodynamic consistency of a Scharfetter-Gummel scheme based on a modified thermal voltage for drift-diffusion equations with diffusion enhancement. *Optical and Quantum Electronics*, 47(6):1327–1332, 2015.

[22] G. Paasch and S. Scheinert. Charge carrier density of organics with Gaussian density of states: Analytical approximation for the Gauss-Fermi integral. *J. Appl. Phys.*, 107(10):104501, 2010.

[23] M. Patriarca, P. Farrell, J. Fuhrmann, and T. Koprucki. Highly accurate quadrature-based Scharfetter-Gummel schemes for charge transport in degenerate semiconductors. *Submitted*, 2018.

[24] Y. Roichman and N. Tessler. Generalized Einstein relation for disordered semiconductors–implications for device performance. *Applied Physics Letters*, 80(11):1948–1950, 2002.

[25] H.-G. Roos, M. Stynes, and L. Tobiska. *Numerical methods for singularly perturbed differential equations: convection-diffusion and flow problems*. Springer Series in Computational Mathematics. Springer, Berlin, Heidelberg, New York, 1996.

[26] D. Scharfetter and H. Gummel. Large-signal analysis of a silicon read diode oscillator. *IEEE Transactions on Electron Devices*, 16(1):64–77, Jan 1969.

[27] S. Selberherr. *Analysis and simulation of semiconductor devices*. Springer, Wien, New York, 1984.

[28] G. Strang and G. Fix. *An Analysis of the Finite Element Method*. Wellesley-Cambridge Press, 2008.

[29] M. Stynes. Steady-state convection-diffusion problems. *Acta Numerica*, 14:445–508, 5 2005.

[30] S. L. M. van Mensfoort and R. Coehoorn. Effect of Gaussian disorder on the voltage dependence of the current density in sandwich-type devices based on organic semiconductors. *Physical Review B*, 78(8), Aug 2008.

[31] M. Zlámal. Finite element solution of the fundamental equations of semiconductor devices. i. *Mathematics of Computation*, 46(173):27–27, Jan 1986.